A Study of Two Numerical Solution Procedures for the Electric Field Integral Equation at Low Frequency

Wen-Liang Wu, Allen W. Glisson, and Darko Kajfez
Dept. of Electrical Engineering
University of Mississippi
University, MS 38677

Abstract *- The numerical solution of the Electric Field Integral Equation (EFIE) using two different low frequency formulations is investigated. The two procedures are implemented for the triangular patch modeling procedure and results obtained for both methods are compared with the original triangular patch EFIE solution. The comparisons are made on the basis of the computed current values and the inverse condition number of the moment matrix. It is observed that the condition number of the matrix can be significantly different between the two low frequency formulations and that the method used to evaluate the forcing function can affect the results both in the low and high frequency ranges.*

I. Introduction

The commonly used numerical solution procedure for the Electric Field Integral Equation (EFIE) has been found to become inaccurate in the frequency range where the maximum dimension of the surface is much smaller than a wavelength [1,2]. The problem arises in the evaluation of the elements of the impedance matrix in the moment method solution procedure, because, if the mixed potential form of the EFIE is used as an example, one observes that $|j\omega A| \ll |\nabla\Phi|$, as $\omega \to 0$. Thus, for a fixed precision computation, the information on the magnetic vector potential A is lost when the frequency is low enough, and the remaining information from the electric scalar potential is not sufficient to determine the surface current distribution. Consequently, the solution is numerically unstable.

This problem may be partially overcome by simply increasing the numeric precision used in the computer code. However, to obtain an EFIE solution that has the potential to be stable at any frequency, a special method of moments solution procedure must be used.

In the following sections, two low-frequency formulations, referred to here as the Loop/Tree and Loop/Star formulations, are presented. These two formulations have been previously studied and have been applied to different method of moments solution procedures [1-5]. Wilton and Glisson first observed the low-frequency problem of the EFIE and applied the Loop/Tree approach as the new testing procedure for a rectangular-patch model of a perfectly electrically conducting plate [1]. Mautz and Harrington explored in greater detail why the numerical solution becomes inaccurate in the low frequency range, and they applied a procedure equivalent to the Loop/Star formulation to their body of revolution code [2]. Lim, Rao, and Wilton applied the Loop/Star procedure to their triangular patch model [3]. Recently, Wu, Glisson, and Kajfez applied both the Loop/Tree and Loop/Star formulations to another triangular patch model and compared results obtained using the two procedures [4,5].

This paper is an extension of [4,5] and sums up our recent research on this topic. A new version of the patch code, referred to here as LFPATCH, has been developed to apply either the Loop/Tree or Loop/Star formulation to extend a version of the patch code [6] to the low frequency range. The modifications for both formulations require the use of different expansion and testing functions that tend to decouple the electrostatic and magnetostatic portions of the solution. A Galerkin testing procedure is used to obtain the system of linear equations. The two different formulations are compared with each other and with the original triangular patch code with regard to accuracy. The two low-frequency formulations, the Loop/Tree and Loop/Star, are described in Section II. The influence of the form of the forcing function on the solution for the low-frequency formulations is discussed in Section III. The numerical results are shown in Section IV to demonstrate the improvement of the stability of the impedance matrix and the accuracy of the computed current density. A summary is provided in Section V.

II. Low-Frequency Formulations

The scattering problem of a perfectly electrically conducting (PEC) body subject to illumination by a time harmonic incident plane wave can be formulated via the EFIE as

$$E^i_{tan}(r) = [j\omega A(r) + \nabla\Phi(r)]_{tan} , \quad r \text{ on } S \qquad (1)$$

where E^i represents the incident electric field, S is the surface of the scatterer, and the subscript *tan* denotes the component of a quantity tangential to the surface S. A and Φ are the magnetic vector potential and the electric scalar potential defined by

$$A(r) = \mu \int_S J(r')G(r,r')dS' , \quad r' \text{ on } S \qquad (2)$$

$$\Phi(r) = \frac{1}{\epsilon} \int_S \sigma(r')G(r,r')dS' , \quad r' \text{ on } S \qquad (3)$$

where

$$G(r,r') = \frac{e^{-jk|r-r'|}}{4\pi|r-r'|} \qquad (4)$$

and where $k = \omega(\mu\epsilon)^{1/2}$, and μ and ϵ are the permeability and permittivity of the surrounding medium. The surface charge density σ is related to the surface divergence of J through the equation of continuity

$$\nabla \cdot J = -j\omega\sigma \qquad (5)$$

Many method of moments [7] schemes have been developed to obtain the numerical solution for equation (1). One of these is the triangular patch model [6], which is based on a method of moments solution of the EFIE in conjunction with a planar triangular patch model of the scatterer and a special set of basis functions. In this section, for completeness, we first describe the basis function used in the original patch code [6]; then the two other vector basis function sets that are suitable for low-frequency use are described.

In the method of moments solution procedure, the surface current density J is approximated as

$$J \cong \sum_{n=1}^{N} I_n u_n(r) \qquad (6)$$

where N is the number of unknowns, I_n is an unknown coefficient to be determined, and u_n is a vector basis function. For the formulation described here, u_n in (6) is chosen from one of three different sets of basis functions: $\{f_n\}$, $\{J_n^L \text{ and } J_n^S\}$, or $\{J_n^L \text{ and } J_n^T\}$. These three sets of basis functions are briefly described in following.

The original vector basis function f_n

As in [6], f_n is a vector basis function defined on a pair of adjacent triangles $T_n^{\pm}$ associated with the n^{th} non-boundary edge of the model, as shown in Figure 1 and defined by equation (7), where l_n is the length of n^{th} edge and $A_n^{\pm}$ is the area of triangle $T_n^{\pm}$.

$$f_n(r) = \begin{cases} \dfrac{l_n}{2A_n^+}\rho_n^+ , & r \text{ in } T_n^+ \\ \dfrac{l_n}{2A_n^-}\rho_n^- , & r \text{ in } T_n^- \\ 0 , & \text{otherwise} \end{cases} \qquad (7)$$

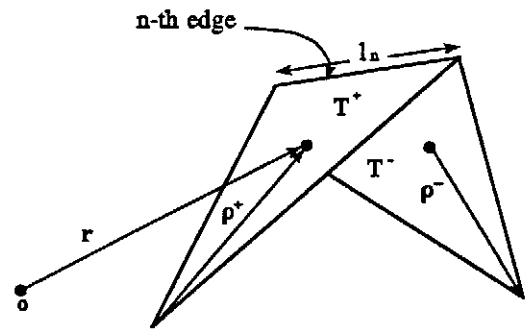

Figure 1. Local coordinates associated with an edge.

To extend the original patch code [6] to the low frequency range, vector basis functions are presented based on the work in [1-3]. These new vector basis functions J_n are divided into two types, J_n^L and either J_n^S or J_n^T, with the following properties which make them suitable for use in the magnetic vector and electric scalar potentials at low frequencies:

- J_n^L is associated with interior nodes and is divergenceless;
- J_n^S is associated with faces and is curl-free;
- J_n^T is equivalent to f_n, but is only associated with the interior edges of the model that lie along a tree structure connecting the centroids of the triangular patches.

The combination of J_n^L and J_n^S is subsequently referred to as the Loop/Star basis function set, and the combination of J_n^L and J_n^T is referred to as the Loop/Tree basis function set. Each of the basis functions J_n^L, J_n^S, and J_n^T can be constructed as a linear combination of the vector basis functions f_n defined in (7).

The vector basis function J_n^L

Figure 2 illustrates in a simplified form the "Loop" basis function J_n^L associated with an interior node n^L. Within each triangle attached to node n^L, J_n^L has vector direction parallel to the edge opposite to node n^L and, therefore, J_n^L forms a loop around node n^L. In Figure 2(a), aside from the edges which are opposite node n^L, all the other edges are connected to node n^L. The currents at these edges connected to node n^L would be unknowns in the original patch code and each would be associated with an original vector basis functions f_n. To obtain the vector basis function J_n^L associated with the interior node n^L, basis functions f_n are first associated with the edges connected to node n^L and are then combined together in a particular manner, so that only a single basis function having zero divergence remains. Figure 2(b) shows the edges and local coordinates associated with one of the triangles in Figure 2(a). In Figure 2(b), if node 1 corresponds to node n^L in Figure 2(a), then J_n^L in this triangle is parallel to edge 1. As indicated in [6], a constant vector of arbitrary magnitude and direction within the triangle may be synthesized by a linear combination of two of the original vector basis functions. Thus, in conjunction with the definition of the vector basis function in equation (7), a vector L_1 within the triangle of Figure 2(b) can be formed as

$$L_1 = \frac{2A}{l_2} f_2 - \frac{2A}{l_3} f_3 \qquad (8)$$

where l_2 and l_3 are the lengths of edges 2 and 3, respectively, and A is the triangle area.

The basis function J_n^L in the triangle of Figure 2(b) is then defined to be

$$J_n^L = \frac{L_1}{A} \qquad (9)$$

This definition holds for all triangles attached to interior node n^L by using the local coordinate notation in Figure 2(b) for each triangle attached to node n^L. Then the basis function J_n^L associated with interior node n^L is defined as

$$J_n^L = \sum_{j=1}^{N_t} \frac{L_j}{A_j} \qquad (10)$$

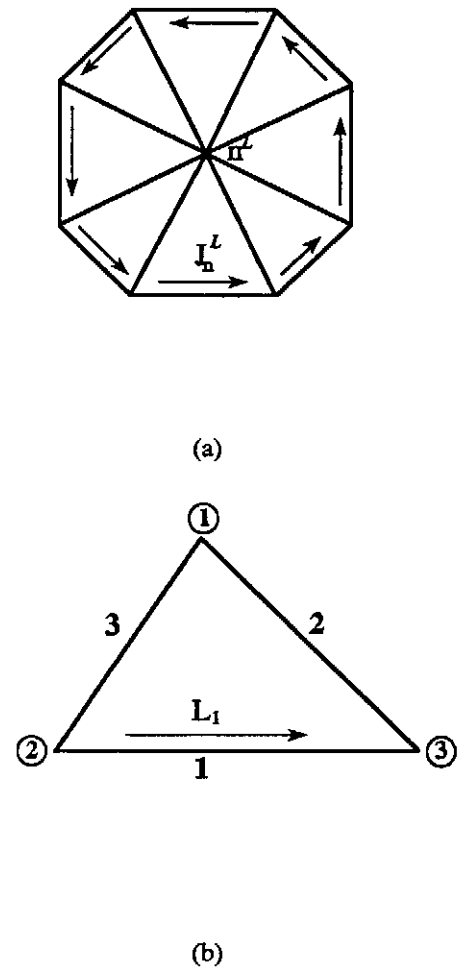

Figure 2. A representation of the vector basis function J_n^L associated with an interior node n^L.

where N_t is the number of triangles attached to node n^L, L_j is the vector parallel to the edge opposite to node n^L in the j^{th} triangle, and A_j is the area of the j^{th} triangle. We note that the triangular patch loop basis function of (10) has been previously used in the computation of polarizabilities for conducting disks and apertures [8] and for magnetostatic solutions for arbitrarily shaped bodies [9].

The vector basis function J_n^S

The "Star" vector basis function J_n^S of [3] is associated with faces and is shown in a simplified representation in Figure 3. The domain of the basis function J_n^S associated with the n^{th} triangular face consists of the n^{th} face itself and all of the faces attached to the n^{th} face. The new basis function is constructed by first placing an original basis function f_n on the triangle pair associated with each edge of

the n^{th} face and orienting these f_n's so that current flows out of the n^{th} face for each one. Finally, the "Star" basis function is formed by summing over the f_n's to obtain

$$J_n^S = \sum_{i=1}^{3} \frac{S_{ni} f_{ni}}{\ell_{ni}} \tag{11}$$

where f_{ni} is an original vector basis function associated with edge i of the n^{th} face, and S_{ni} is a sign and magnitude coefficient chosen from the set {-1, 0, 1} to provide current flow out of the n^{th} face for a non-boundary edge i or to eliminate contributions from boundary edges.

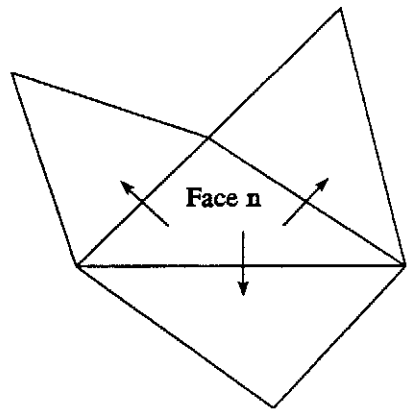

Figure 3. A representation of the vector basis function J_n^S associated with a triangular patch.

The vector basis function J_n^T

The "Tree" basis function J_n^T consists of the f_n's for the interior edges of the model that lie along a tree structure connecting the centroids of adjacent triangular patches. The definition of *tree* and *branch* for the rectangular-patch model in [Ch.8, 10] is also applied for the triangular patches used here. A possible choice of the tree for a triangular patch model is shown in Figure 4. Once a tree is obtained, J_n^T can be defined as

$$J_n^T = \begin{cases} f_t \text{ , } \textit{if edge } t \textit{ intersects a tree branch} \\ 0 \text{ , } \textit{otherwise} \end{cases} \tag{12}$$

where f_t is the original vector basis function associated with a non-boundary edge t.

With these definitions, three simple approaches are used to form a complete set of basis functions. The surface current density J is then approximated by either of the three basis function sets. If the set of original vector basis functions f_n is chosen, i.e., if the same basis set as in [6] is used, then

$$J(r) \cong \sum_{n=1}^{N} I_n f_n(r) \tag{13}$$

where N is the number of interior (non-boundary) edges in the triangular patch model. If the Loop/Star basis function set is chosen, then J is represented as

$$J(r) \cong \sum_{n=1}^{N^L} I_n J_n^L(r) + \sum_{n=N^L+1}^{N} I_n J_n^S(r) \tag{14}$$

where N^L is the number of interior nodes, and $N - N^L + 1$ is the number of faces in the triangular patch model. If the Loop/Tree basis function set is chosen instead, then

$$J(r) \cong \sum_{n=1}^{N^L} I_n J_n^L(r) + \sum_{n=N^L+1}^{N} I_n J_n^T(r) \tag{15}$$

where $N - N^L$ is the number of tree branches in the triangular patch model.

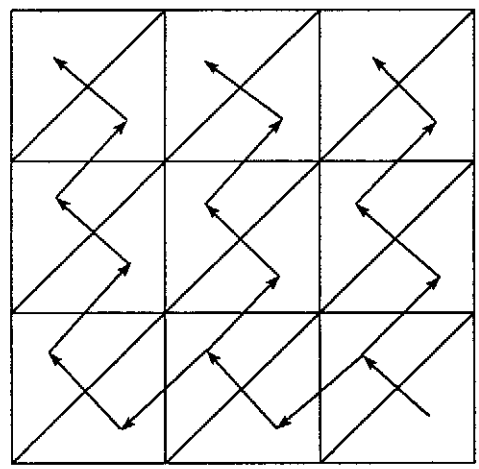

Figure 4. A tree structure connecting the centroids of adjacent triangular patches.

The basis function set J_n^L must include an additional type of element if the body being modeled is not simply connected, as shown in Figure 5. The connectivity of the body can be determined from the triangular patch model for some classes of geometries by noting, for example, that the triangular patch model of a simply connected open surface without any "handles" will have either no "aperture" or only one "aperture," i.e., either there will be no boundary edge or the union of all of the boundary edges in the patch model will form a single closed curve. For each additional aperture in the model it is necessary to include a "super-loop" basis function of form similar to J_n^L. These

additional basis functions will form loops around apertures rather than around interior nodes of the model. In Figure 5, the surface modeled by triangular patches has two apertures; therefore, an additional "super-loop" basis function is needed if one uses one of the low-frequency formulations to determine the surface current. Additional "super-loop" basis functions are also needed if a body modeled by triangular patches has any "handles," as is the case for a closed body that is not simply connected, such as a torus, or for the general open-body geometry illustrated in [6]. The definition and topological properties of a "handle" can be found in [11]. The construction of a "super-loop" basis function is similar to that of Loop basis function f_n^L. The only difference is that the Loop basis function f_n^L is formed by all f_n's attached to node n^L, while a "super-loop" basis function can be formed by all the f_n's associated with edges that are attached to an appropriate aperture (either aperture 1 or aperture 2 in Figure 5, for example).

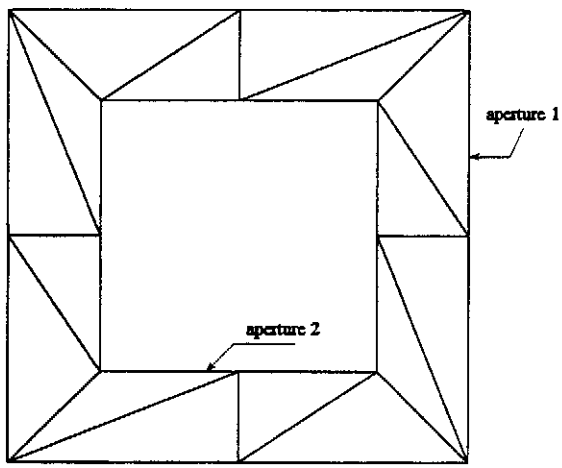

Figure 5. An object with two apertures.

With a Galerkin testing procedure, the impedance matrix elements for the three different basis function sets may be represented as

$$[Z_{orig}]_{mn} = j\omega \langle A(f_n), f_m \rangle + \langle \frac{j}{\omega} \nabla\Phi(\nabla_s \cdot f_n), f_m \rangle \quad (16)$$

$$[Z_{L/S}]_{pq} = \begin{bmatrix} B_{nm}^{LL} & B_{nm}^{SL} \\ B_{nm}^{LS} & B_{nm}^{SS}+C_{nm}^{SS} \end{bmatrix} \quad (17)$$

$$[Z_{L/T}]_{pq} = \begin{bmatrix} B_{nm}^{LL} & B_{nm}^{TL} \\ B_{nm}^{LT} & B_{nm}^{TT}+C_{nm}^{TT} \end{bmatrix} \quad (18)$$

with

$$B_{nm}^{st} = j\omega \langle A(J_n^s), J_m^t \rangle$$

$$C_{nm}^{st} = \langle \frac{j}{\omega} \nabla\Phi(\nabla_s \cdot J_n^s), J_m^t \rangle$$

where the superscripts s,t may be either L, S, or T and indicate the source and testing function types, and $\langle\ \rangle$ denotes the symmetric product. The brackets on the right side of (17) and (18) indicate that the matrix element is given by one of the expressions for the four different subtypes of matrix elements arising due to the two different basis and testing function types, the local subscripts m and n in (17) and (18) are assumed to be mapped appropriately into the global matrix indices p and q, and the subscripts *orig*, *L/S*, and *L/T* on Z denote the basis and testing function types. Equation (16) uses the original basis and testing functions; equation (17) uses the Loop/Star basis and testing functions; and equation (18) uses the Loop/Tree basis and testing functions.

If one compares equations (17) and (18) with (16), it is evident that the magnetic vector potential contribution to the elements of the impedance matrix appears alone in the upper portions of $Z_{L/S}$ and $Z_{L/T}$, and, therefore, is not lost in comparison with $|\nabla\Phi|$ during matrix element computation. We also note that the low-frequency formulations described in this section are valid in principle at any non-zero frequency.

III. The Forcing Function for Low-Frequency Formulations

When a Galerkin testing procedure is applied to equation (1), the left side yields the forcing function, or excitation vector $|V\rangle$ for the system of equations. Four different types of excitation vector elements can be obtained by using f_n, J_n^L, J_n^S, or J_n^T, as described in the last section. If the original basis function f_n is used as the testing function, the same excitation vector as in [6] is obtained

$$V_m^{orig} = \langle E^{inc}, f_m \rangle = \int_S E^{inc} \cdot f_m \, dS \quad (19)$$

where $m = 1,2,\ldots,N$, and N is the number of interior (non-boundary) edges in the triangular patch model. For simplicity in the numerical calculation, E^{inc} is often approximated by the corresponding value of E^{inc} at the centroid of each triangle. If J_n^T is used as the testing function, then

$$V_p^T = \begin{cases} V_t^{orig} \text{ , if edge } t \text{ intersects a tree branch} \\ 0 \text{ , otherwise} \end{cases} \quad (20)$$

where $p = 1,2,\ldots,N\text{-}N^L$ is the p^{th} tree branch, and N^L is the number of interior nodes in the triangular model. If J_n^S is used as the testing function, then

$$V_q^S = \sum_{i=1}^{3} \frac{S_{qi} V_{qi}^{orig}}{\ell_{qi}} \quad (21)$$

where $q = 1,2,\ldots,N^{star}$, N^{star} is the number of unknowns associated with the Star basis function, and S_{qi} is a sign coefficient chosen in the same manner as for (11).

It is evident that we use the same strategy to form the excitation vectors $|V^T>$ and $|V^S>$ as we did in last section to develop the *Tree* and *Star* basis functions. But when J_n^L is used as the testing function, there are two ways to evaluate the excitation vector $|V^L>$. In the first approach, we use a linear combination of the V_m's given in equation (19) to construct the excitation vector $|V^L>$. Applying the same procedure as for the construction of the *Loop* basis function in last section, we obtain

$$V_i^{Lei} = \sum_{j=1}^{N_t} \left(\frac{2V_2^{orig}}{l_2} - \frac{2V_3^{orig}}{l_3} \right) \quad (22)$$

where V^{orig} is given in equation (19), $i = 1,2,\ldots,N^L$, N_t is the number of triangles attached to i^{th} the interior node n^L in the triangular patch model, and the subscripts 2 and 3 refer to local edge numbers as in Figure 2. The superscript *Lei* denotes the testing function is a *Loop* testing function, and that the incident electric field is used in the calculation. In the second approach, we start with the symmetric product expression for the excitation vector with the *Loop* as the testing function:

$$V_i^{Lhi} = <E^{inc}, J_i^L> = \sum_{j=1}^{N_t} \int_S E^{inc} \cdot J_i^L \, dS \quad (23)$$

Using a vector calculus identity [12], equation (23) can be written as

$$V_i^{Lhi} = \sum_{j=1}^{N_t} \int_S \psi_j \, \hat{n} \cdot (\nabla \times E^{inc}) \, dS \quad (24)$$

which can be further manipulated to

$$V_i^{Lhi} = -j\omega\mu \sum_{j=1}^{N_t} \int_S \psi_j \, (\hat{n} \cdot H^{inc}) \, dS \quad (25)$$

where ψ_j is a scalar function [9] defined over the j^{th} triangle attached to node n^L (cf. Figure 2), and H^{inc} is the incident magnetic field. If H^{inc} is approximated by the corresponding values of H^{inc} at the centroids of each triangle attached to node n^L, then

$$V_i^{Lhi} = -j\omega\mu \frac{2}{3} \sum_{j=1}^{N_t} A_j \, \hat{n} \cdot H^{inc}(r_j^c) \quad (26)$$

where A_j is the area of the j^{th} triangle attached to node n^L and r_j^c is the position vector to the centroid of the j^{th} triangle. The superscript *Lhi* denotes that the testing function is a *Loop* testing function, and that the incident magnetic field is used in the calculation. This result is similar to that obtained by Arvas *et al* [9], where the magnetostatic problem was solved. It is apparent from (23) to (25) that testing the incident field with the *Loop* testing function is equivalent to performing a curl operation. Comparing $|V^{Lei}>$ of (22) with $|V^{Lhi}>$ of (26), one notes that $|V^{Lei}>$ effectively evaluates the curl of E^{inc} numerically, while for $|V^{Lhi}>$ the curl operation is performed through the analytic procedure (23) to (25). In principle, either $|V^{Lei}>$ or $|V^{Lhi}>$ can serve as the excitation vector. However, the numerical results have demonstrated that computational advantages can be gained by using $|V^{Lei}>$ in the higher frequency range and by choosing $|V^{Lhi}>$ when the operation frequency is in the lower frequency range (i.e., when the scatterer is very small in terms of wavelength). This is not surprising, since evaluation of $|V^{Lei}>$ over a loop results in substantial cancellation of the electric field vector over the testing path and a subsequent loss of precision when the testing path is small in terms of wavelength. Numerical results demonstrating these effects and further discussion are presented in the next section.

IV. Numerical Results

The two low-frequency vector basis functions described in the previous sections have been incorporated in a version of the patch code [6]. This new version of the patch code is referred to here as LFPATCH, which stands for Low Frequency triangular patch code. To study the behavior of the code for the different approaches, several structures have been studied over a wide frequency range. Numerical results are presented in this section comparing the inverse of the condition numbers [13] of the impedance matrix and current distributions obtained using the different basis

function sets. All the scatterers studied are modeled by triangular patches and subject to illumination by an incident plane wave.

To observe the effects of numerical precision of different computers, the examples are computed on different platforms with different precision. The two platforms used for the numerical computations are an IBM 3084QXC Mainframe and a Cray Y-MP8D/464 Supercomputer. The Cray single precision computation is effectively equivalent to the double precision computation on the IBM mainframe.

Flat Square Plate Scatterer

The first example problem considered is a square, flat plate PEC scatterer illuminated by an incident wave with the *H* component normal to the surface of scatterer, as shown in Figure 6. The inverse condition number obtained for the

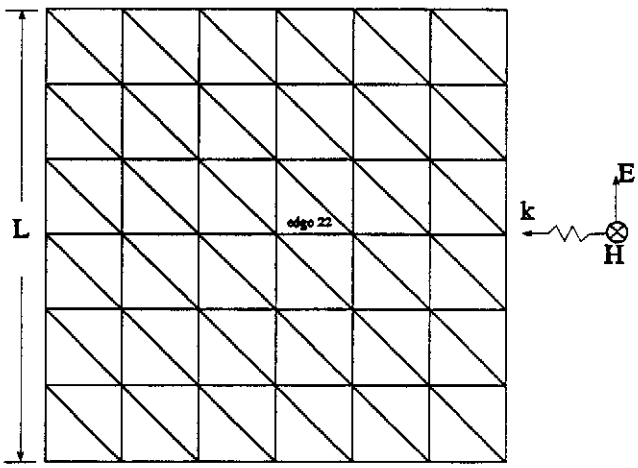

Figure 6. A triangular patch model of a flat square plate scatterer.

impedance matrix using the original, Loop/Tree, and Loop/Star basis function sets are shown in Figure 7. Figure 7(a) shows the inverse condition number for the three basis function sets obtained by running the code on the IBM mainframe using single precision, and Figure 7(b) shows the same case, but running on the Cray supercomputer. The inverse condition number for the impedance matrix using the original basis function set is found to start oscillating wildly when L/λ is smaller than about 10^{-3} for the IBM single precision result. When the impedance matrix is evaluated on the Cray, there is no oscillation, but there is a clear change in the behavior of the curve at $L/\lambda = 10^{-6}$. The inverse condition numbers for the two low-frequency formulations are essentially constant as a function of

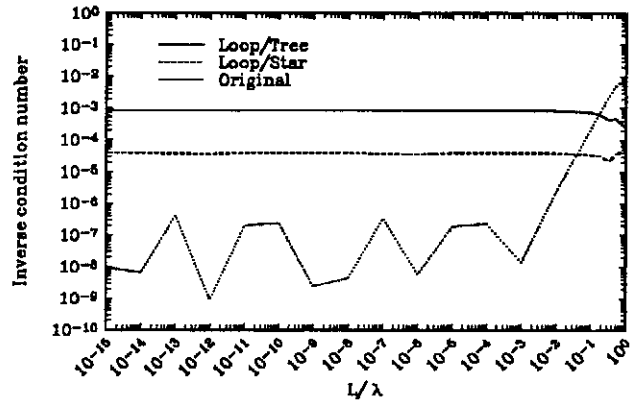

Figure 7(a). Inverse condition number for a square plate scatterer obtained using single precision on the IBM mainframe.

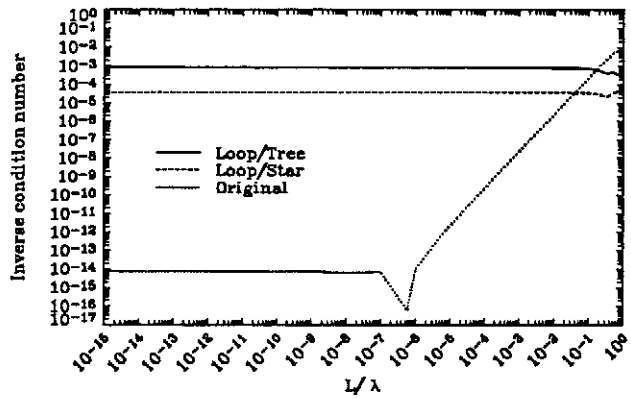

Figure 7(b). Inverse condition number for a square plate scatterer obtained using single precision on the Cray supercomputer.

frequency for L/λ smaller than about 10^{-2} regardless of the platform used. It is also noticed that the condition number obtained with the Loop/Tree basis function is more than an order of magnitude better than that obtained with the Loop/Star basis function.

The effect of using either $|V^{Lei}>$ or $|V^{Lhi}>$ on the computed current distribution for the flat plate scatterer is shown in Figures 8 and 9. The data for both Figures 8 and 9 were generated on the Cray supercomputer. Figures 8(a) and 9(a) show the absolute value of the real and imaginary parts of the current coefficient for edge 22 of the model (Figure 6) over a wide frequency range, while Figures 8(b) and 9(b) show an expanded plot over the higher portion of the frequency range. One observes from Figure 8(a), for which $|V^{Lei}>$ is used, that good agreement is obtained for

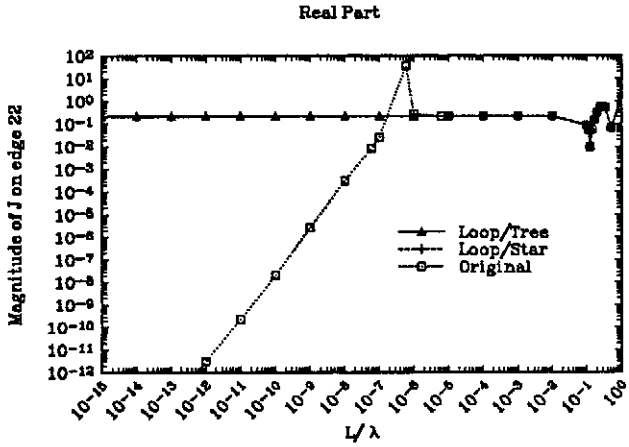

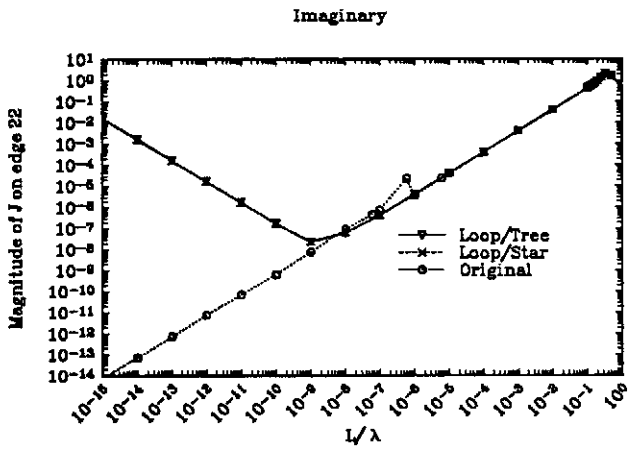

Figure 8(a). Current density at edge 22 for the flat plate scatter obtained using the excitation vector $| V^{Lei} >$.

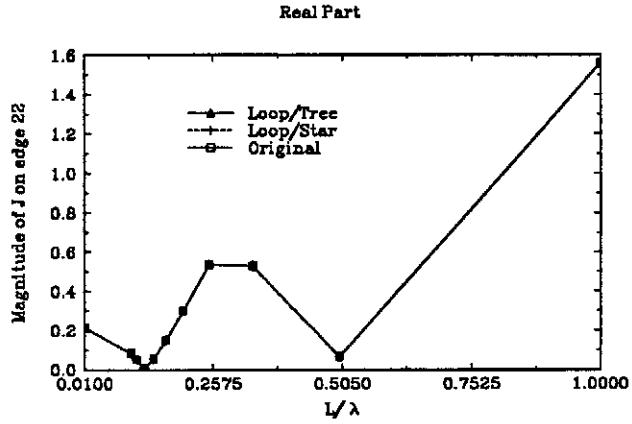

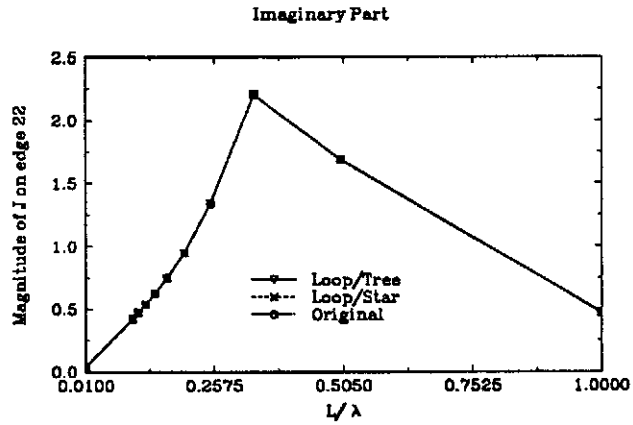

Figure 8(b). Current density at edge 22 for the flat plate scatter obtained using the excitation vector $| V^{Lei} >$ (high frequency range).

the real part of the current using the two low-frequency formulations; however, the result obtained using the original basis function becomes erratic at the frequency where the impedance matrix becomes unstable (see Figure 7(b)). The imaginary part of the current obtained with the two low-frequency approaches, on the other hand, becomes inaccurate for L/λ smaller than about 10^{-8}, where one notes that the computed current begins to rise as the frequency decreases. If we use $| V^{Lhi} >$ instead, the result obtained is shown in Figure 9(a). For frequencies such that L/λ less than about 10^{-1}, the real part of the current compares well with the results in Figure 8(a); however, the imaginary part of the current for Loop/Tree and Loop/Star basis functions behaves correctly over this same frequency range, unlike the results of Figure 8(a). Expanded plots of the current obtained using the excitation vectors $| V^{Lei} >$ and $| V^{Lhi} >$ for the two low-frequency approaches over the higher portion of the frequency range are compared with the original EFIE procedure in Figures 8(b) and 9(b). Over the part of the frequency range shown in Figure 9(b), one observes that the currents computed using $| V^{Lhi} >$ do not agree with each other or with the original EFIE. For the same frequency range, the currents obtained using $| V^{Lei} >$ for the two low-frequency approaches, shown in Figure 8(b), are in excellent agreement for both the real and imaginary parts of the current for the three different solution procedures. The results shown in these figures suggest that a different *Loop* testing procedure should be used for the excitation vector calculation for the high and low frequency range. If we consider Figures 8 and 9 again, we can roughly divide the entire frequency range into three

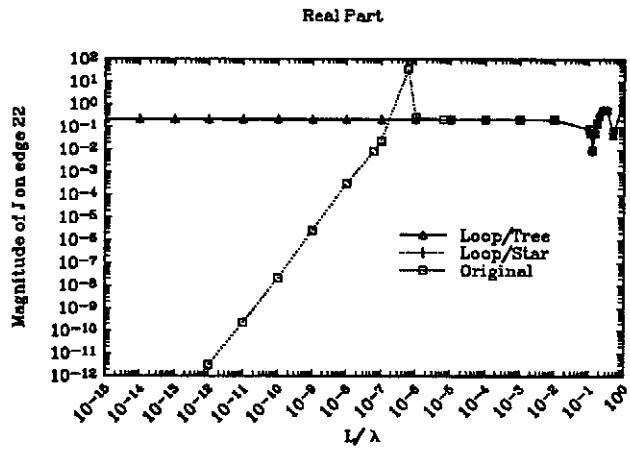

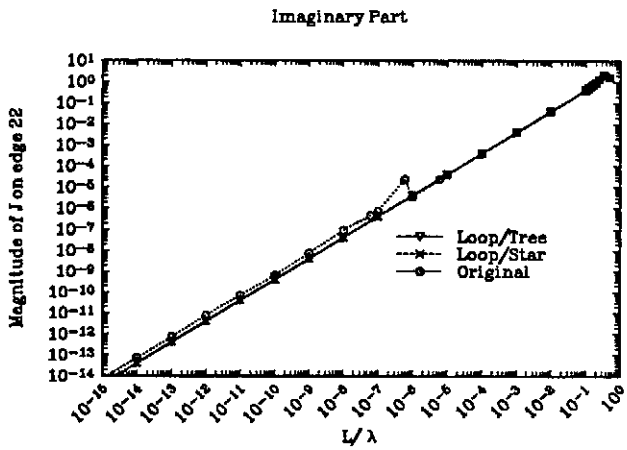

Figure 9(a). Current density at edge 22 for the flat plate scatter obtained using the excitation vector $|V^{Lhi}>$.

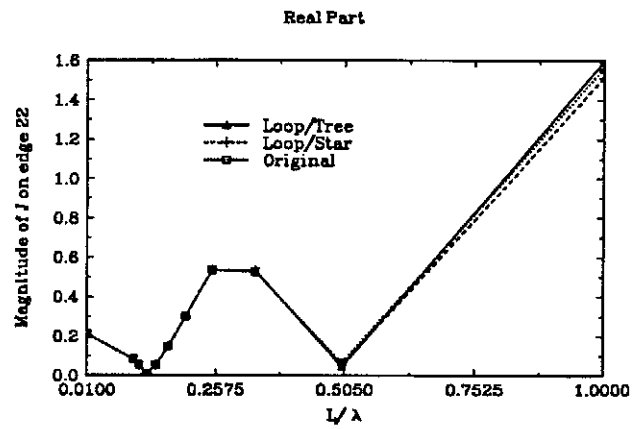

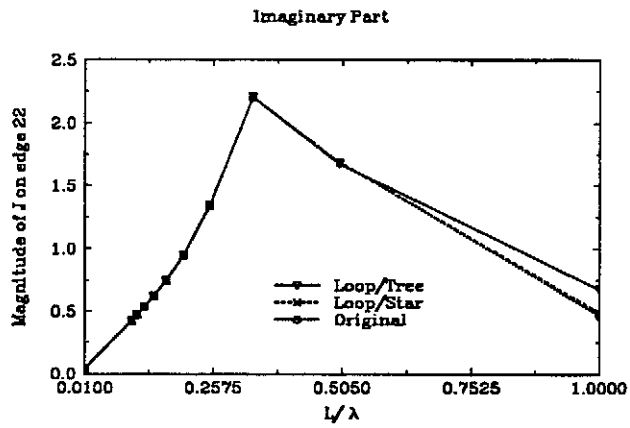

Figure 9(b). Current density at edge 22 for the flat plate scatter obtained using the excitation vector $|V^{Lhi}>$ (high frequency range).

convenient regions: region A, where L/λ varies from 10^0 to 10^{-2}; region B, where L/λ varies from 10^{-2} to 10^{-7}; and region C, where L/λ is smaller than 10^{-7}. In region A, the size of a triangle ($A=0.0139\lambda^2$ at L/λ = 1) is comparable in size with the wavelength. To understand the failure of $|V^{Lhi}>$ in this region, we note that when $|V^{Lhi}>$ was derived in the previous section, an analytic curl operation was performed around the interior node n^L via a vector calculus identity. If one recalls that the integral definition of the curl operation evaluates a vector field as an area tends to zero, which implies the field does not change rapidly around node n^L, it is recognized that the numerical application for this definition may not be appropriate in region A. As the frequency decreases, especially in region C, the size of triangle becomes very small in terms of wavelength, and the value of $|V^{Lhi}>$ becomes quite accurate. The good agreement between all of the approaches in region A for the results obtained when using $|V^{Lei}>$ for two the low-frequency approaches is because all the quantities (A, Φ, E^{inc}) are evaluated at the same points, the triangle centroids, and because there is little loss of numerical accuracy due to cancellation when the triangles are not small with respect to the wavelength. When the frequency falls into region C, the variation of E^{inc} is very small over the domain of the loop basis function ($A=1.39\times10^{-16}\lambda^2$ at L/λ = 10^{-7}), and the testing procedure leads to the subtraction of very similar field quantities, causing a loss of precision in the computation of $|V^{Lei}>$ for the two low-frequency approaches, which leads to unacceptable results. In region B, both $|V^{Lei}>$ and $|V^{Lhi}>$ for two the low-frequency approaches provide essentially the same result. For the results shown

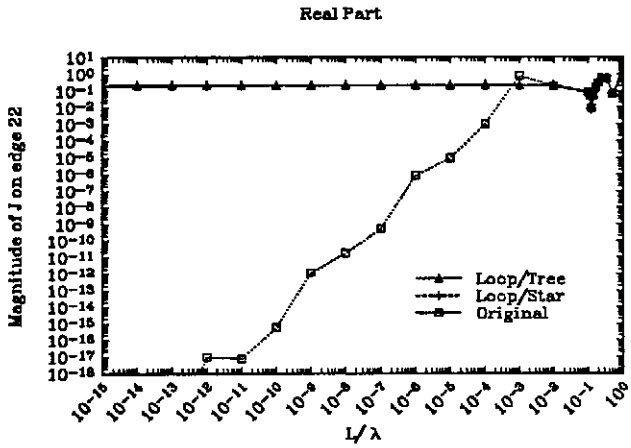

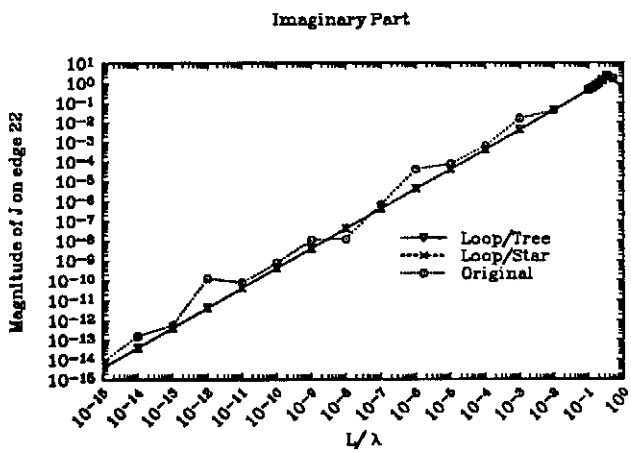

Figure 10(a). Current density at edge 22 for the flat plate scatter obtained using the excitation vector $|V^{Leh}>$ on the IBM mainframe using single precision.

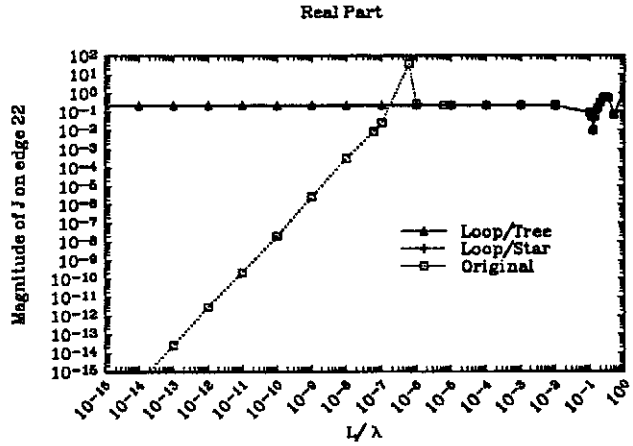

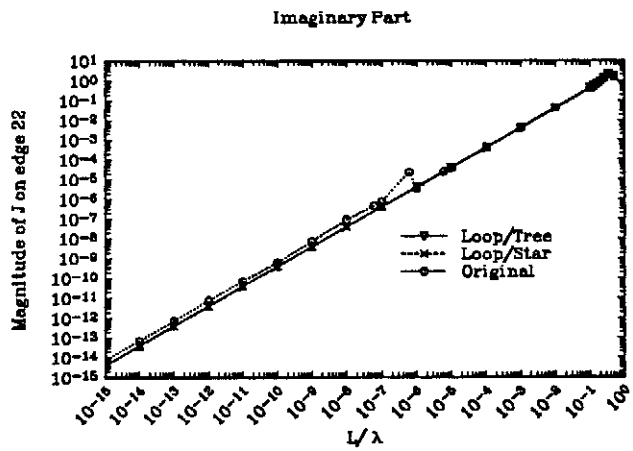

Figure 10(b). Current density at edge 22 for the flat plate scatter obtained using the excitation vector $|V^{Leh}>$ on the Cray supercomputer using single precision.

subsequently, we use $|V^{Lei}>$ in region A, $|V^{Lhi}>$ in region C for the two low-frequency approaches, and switch between the two excitation vectors in region B according to the size of triangle respect to the wavelength. We refer to this as the combined Loop testing procedure, and the corresponding excitation vector is denoted as $|V^{Leh}>$. Figures 10(a) and 10(b) show the current density at edge 22 in Figure 6 obtained using the three basis function sets and on different platforms. Since the $|V^{Leh}>$ is used for the Loop testing function, the results obtained with the two low-frequency approaches now agree with each other over the entire frequency shown and are stable even computed on the IBM mainframe in single precision.

Long Narrow Bent Strip

The next example presented is a long narrow (L=30W) strip which forms a square, open loop, as shown in Figure 11. In this example, to make a simple model with relatively few unknowns for this shape of scatterer, the sizes of triangular patches in the model are not made uniform. Results are shown in Figure 12 for the inverse condition number in this case, and they are similar to those of the previous case, except that the inverse condition number for the Loop/Tree basis function set is now about two orders of magnitude better than that of the Loop/Star basis function set. Consequently, one might expect for this case that the Loop/Tree procedure is the only one likely to provide a reasonable solution with single precision on the IBM

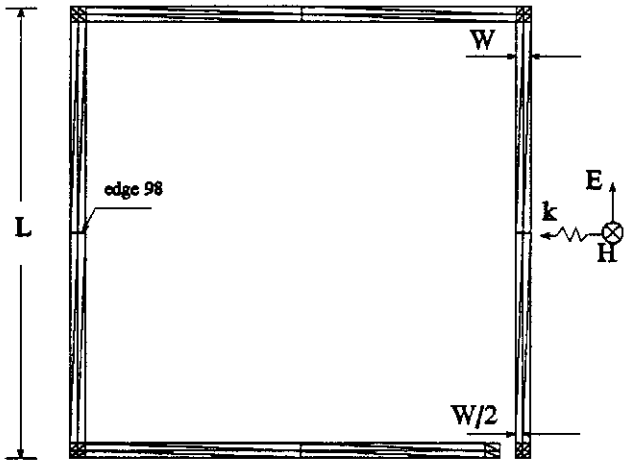

Figure 11. A long narrow bent strip (L=30W).

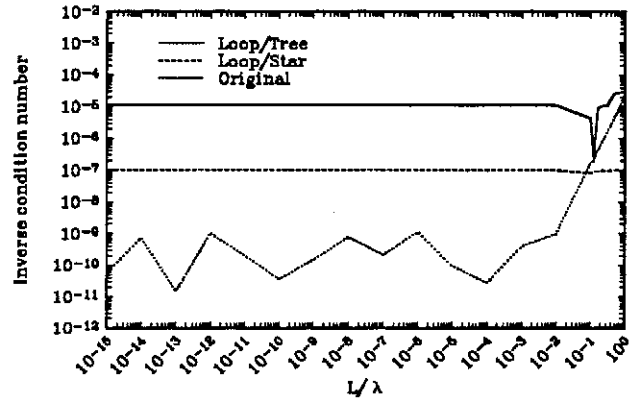

Figure 12(a). Inverse condition number for a long narrow bent strip obtained using single precision on the IBM mainframe.

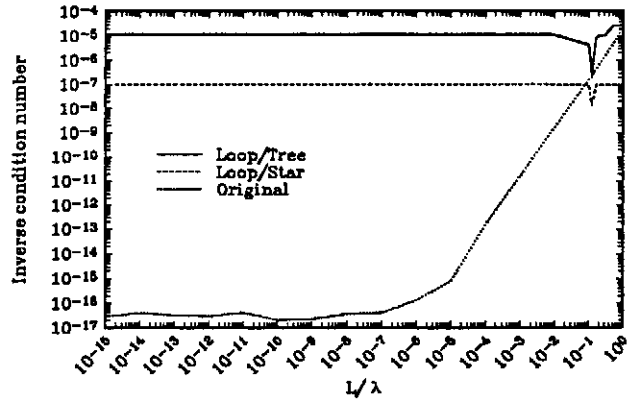

Figure 12(b). Inverse condition number for a long narrow bent strip obtained using single precision on the Cray supercomputer.

mainframe. From Figure 12(b), it can be observed that, as the precision is increased, the the inverse condition number results obtained using both procedures are large enough relative to the machine precision to expect accurate solutions, while that obtained using the original basis function set shows improvement for L/λ larger than about 10^{-6}, but again deteriorates when L/λ becomes smaller than about 10^{-6}. The results for the current on one of the edges shows behavior similar to that of in previous case.

It should be noted here, however, that scaling of the basis functions may affect the matrix conditioning [14]. Indeed, we have observed, for example, that if the edge length factor in the denominator of (11) is omitted, the Loop/Star results are worse by almost an order of magnitude. The Loop basis and testing functions are the same in both low frequency methods. Nevertheless, application of a scaling factor to the Loop functions may improve the Loop/Star and/or the Loop/Tree condition numbers and is a subject for further research.

V. Summary and Discussion

Two special method of moments solution procedures used to improve the accuracy of the numerical solution for the Electric Field Integral Equation (EFIE) in the low frequency range have been studied. Two alternate vector basis functions have been implemented in a version of the triangular patch code [6] to extend its usefulness to the low frequency range. Numerical results have been presented for two different types of structures over a wide frequency range. The inverse condition numbers of the impedance matrix and the computed current values as a function of frequency have been presented to illustrate the improvement of the EFIE solution in the low-frequency range. It has been found in our implementations that using the Loop/Tree basis and testing functions usually yields a more stable impedance matrix (i.e., one with a larger inverse condition number). This is very useful when modeling a resonant structure that is small in terms of wavelength, since near the resonant frequency, the inverse condition number of the impedance matrix usually drops several orders of magnitude from that of the off-resonance case. This is also helpful when the code is running on a computer with lower precision. Additional study of scaling procedures may result in further improvements of the inverse condition numbers of one or both of the low frequency methods.

References

[1] D. R. Wilton and A. W. Glisson, "On improving the electric field integral equation at low frequencies," *1981 Spring URSI Radio Science Meeting Digest*, p. 24, Los Angeles, CA, June 1981.

[2] J. R. Mautz and R. F. Harrington, "An E-field solution for a conducting surface small or comparable to the wavelength," *IEEE Antennas Propagat.*, vol. AP-32, pp. 330-339, April 1984.

[3] J. S. Lim, S. M. Rao, and D. R. Wilton, "A novel technique to calculate the electromagnetic scattering by surfaces of arbitrary shape," *1993 URSI Radio Science Meeting Digest*, p. 322, Ann Arbor, Michigan, June 1993.

[4] W. Wu, A. W. Glisson, and D. Kajfez, "A comparison of two low-frequency formulations for the electric field integral equation," *Proceedings of the 10th Annual Review of Progress in Applied Computational Electromagnetics*, vol. II, pp. 484-491, Monterey, California, March 1994.

[5] W. Wu, A. W. Glisson, and D. Kajfez, "Electromagnetic scattering by resonant low-frequency structures," *1994 URSI Radio Science Meeting Digest*, p. 137, Seattle, Washington, June 1994.

[6] S. M. Rao, D. R. Wilton, and A. W. Glisson, "Electromagnetic scattering by surfaces of arbitrary shape," *IEEE Trans. Antennas Propagat.*, vol. AP-30, pp. 409-418, May 1982.

[7] R. F. Harrington, *Field Computation by Moment Methods*. New York: Macmillan, 1968.

[8] E. Arvas and R. F. Harrington, "Computation of the magnetic polarizability of conducting disks and the electric polarizability of apertures," *IEEE Trans. Antennas Propagat.*, vol. AP-31, pp. 719-724, Sept. 1983.

[9] E. Arvas, R. F. Harrington, and J. R. Mautz, "Radiation and scattering from electrically small conducting bodies of arbitrary shape," *IEEE Trans. Antennas Propagat.*, vol. AP-34, pp. 66-77, Jan. 1986.

[10] C. M. Butler, D. R. Wilton, and A. W. Glisson, *A Short Course on Fundamentals of Numerical Solution Methods in Electromagnetics*, University of Mississippi, October 1984.

[11] S. M. Rao, "Electromagnetic scattering and radiation of arbitrarily-shaped surfaces by triangular patch modeling," Ph.D. dissertation, University of Mississippi, 1980.

[12] J. Van Bladel, *Electromagnetic Fields*. New York: McGraw-Hill, 1964.

[13] R. Mittra and C. A. Klein, "Stability and Convergence of Moment Method Solutions," Chapter 5 in *Topics in Applied Physics*, Volume 3, edited by R. Mittra, Springer-Verlag, 1975.

[14] D. R. Wilton, private communication.